Science Advances
AAAS

Supplementary Materials for

A single-phase epitaxially grown ferroelectric perovskite nitride

Songhee Choi *et al.*

Corresponding author: Kuijuan Jin, kjjin@iphy.ac.cn; Shanmin Wang, wangsm@sustech.edu.cn;
Jiawang Hong, hongjw@bit.edu.cn; Er-Jia Guo, ejguo@iphy.ac.cn

Sci. Adv. **11**, eadu6698 (2025)
DOI: 10.1126/sciadv.adu6698

This PDF file includes:

Figs. S1 to S30
References

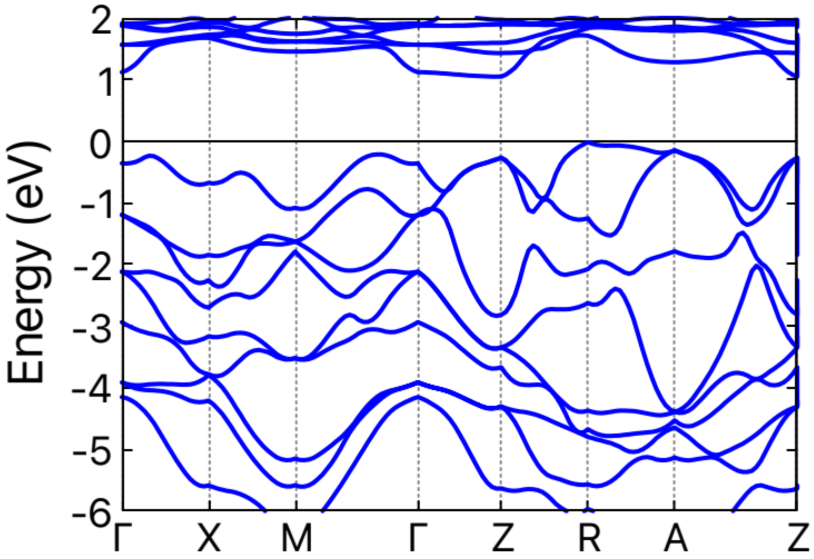

fig. S1. Band structures, as calculated with the HSE06 functional for $CeTaN_3$. The indirect band gaps are indicated. The zero of energy is set at the valence-band maximum.

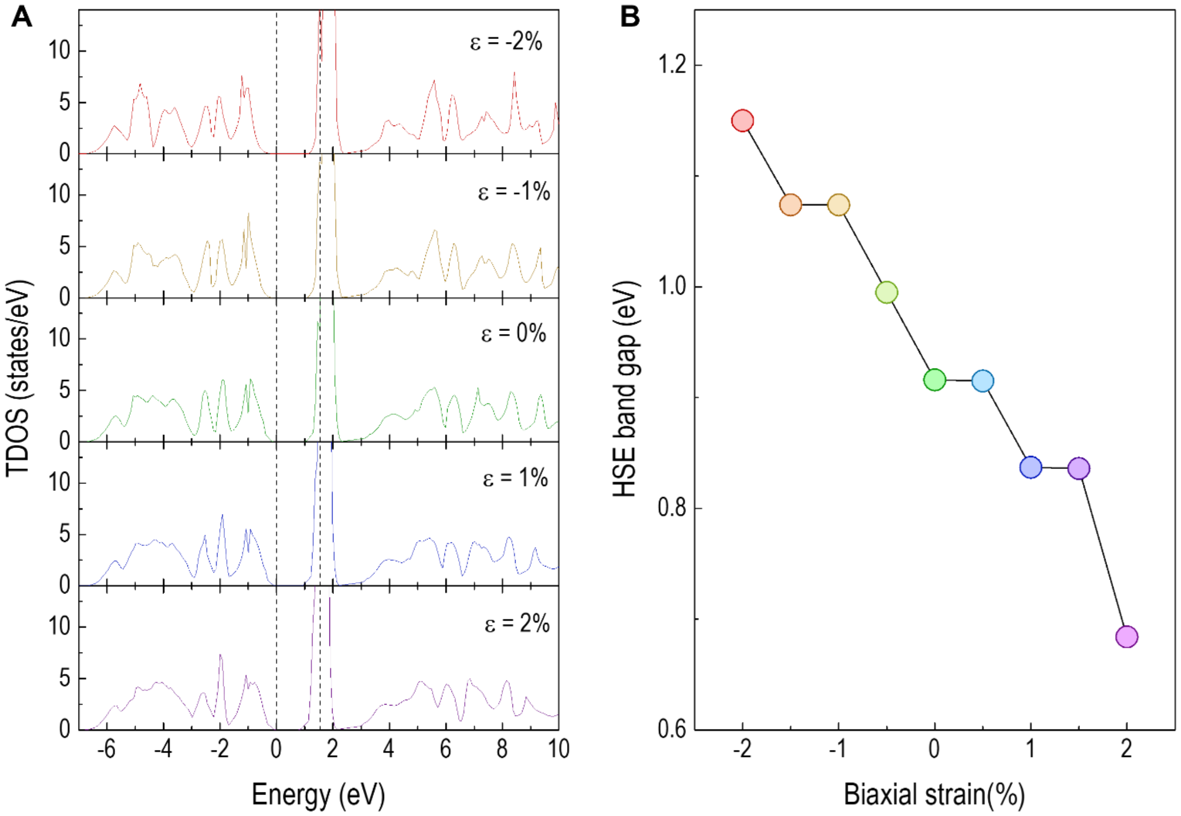

fig. S2. The band gap evolution of $CeTaN_3$ as a function of biaxial strain. (**A**) Total DOS of CeTaN3 with biaxial strain ranging from –2% to 2%. Increasing epitaxial strain reduces the band gap, which is mainly caused by the downward movement of conduction band. (**B**) HSE bandgap evolution as a function of biaxial strain.

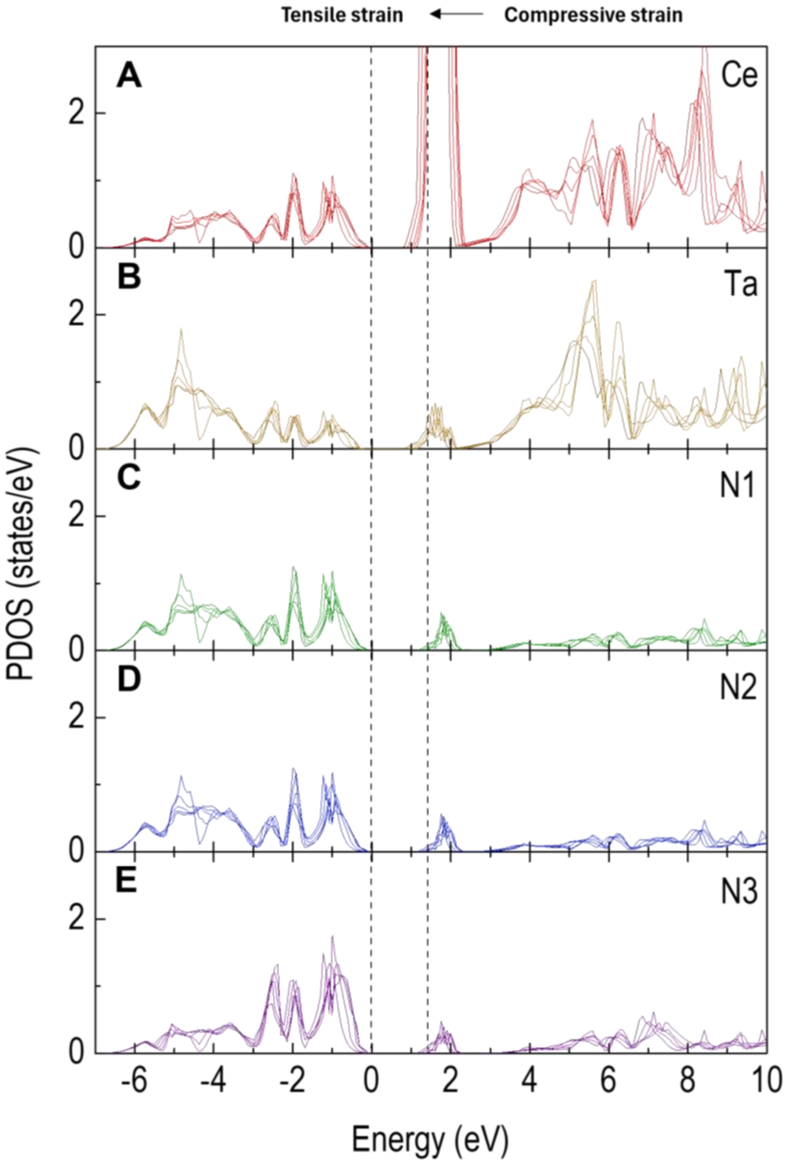

fig. S3. The comparison of PDOS of all elements under different strain states. PDOS of (**A**) Ce, (**B**) Ta, (**C**) N1, (**D**) N2, and (**E**) N3. Biaxial strain produces an additional energy shift to all atoms, leading to a smaller band gap under tensile strain and a larger band gap under compressive strain. Both tensile and compressive strain causes conduction band downward, while only compressive strain causes the valence band upward.

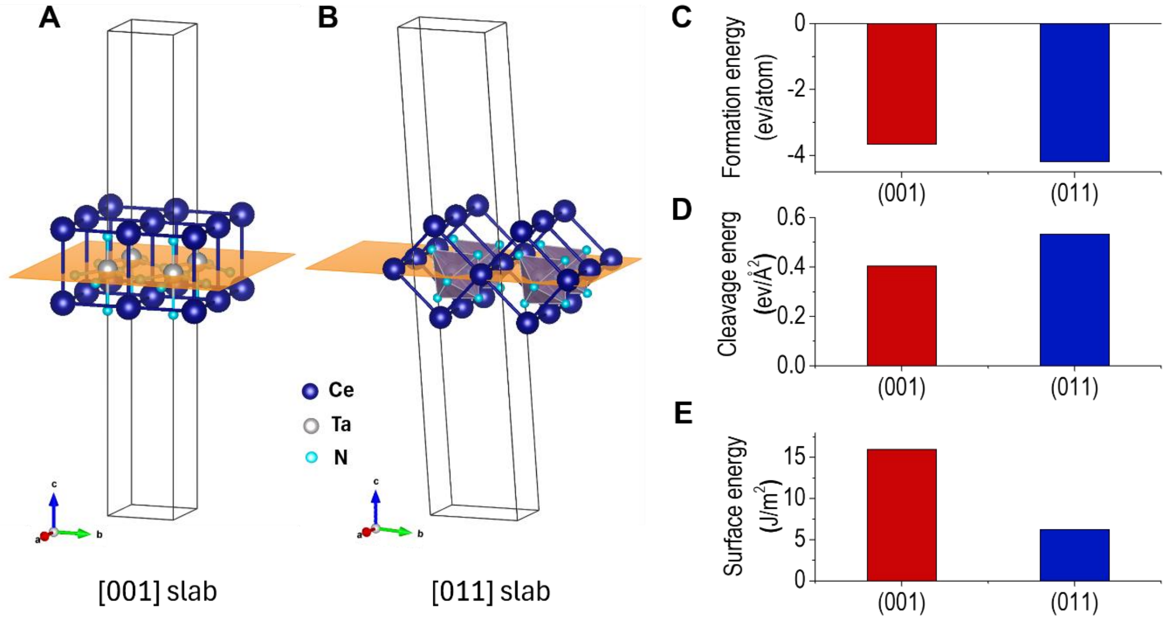

fig. S4. Comparison of formation energy, cleavage energy, and surface energy for (001)-, and (011)-oriented CeTaN$_3$. We can calculate the formation energy Ef by $(E_{slab} - n(E_{Ce} + E_{Ta} + 3 * E_N))/N_{atom}$, the cleavage energy Ecle by $(E_{top}^{unrel} + E_{bottom}^{unrel} - E_{bulk})/2S$, and the surface energy Esurf by (Eslab – nEbulk)/A, where Eslab is the total energy of the relaxed CeTaN$_3$, Ebulk is the total energy of CeTaN$_3$ bulk with the same crystal structure. E_{Ce}, E_{Ta} , and E_N are total energy of single atom of Ce, Ta, and N, respectively. E_{top}^{unrel} is the unrelaxed energy of the top layer after cleavage, E_{bottom}^{unrel} is the unrelaxed energy of the bottom layer after cleavage. All energies can be calculated using first-principles calculations based on density functional theory.

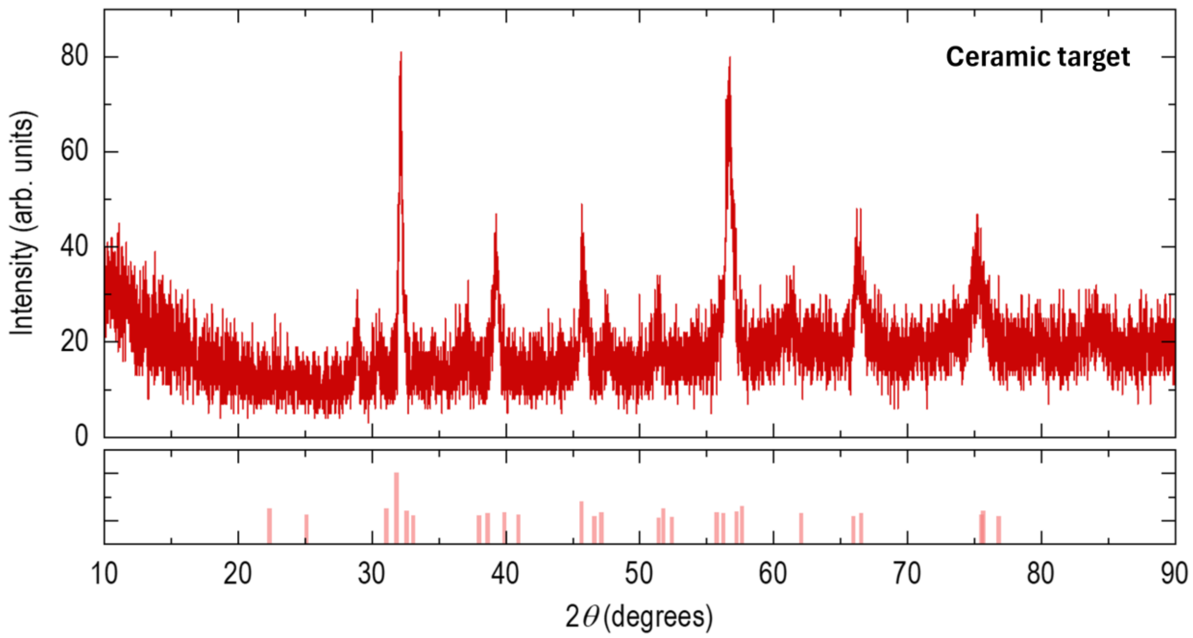

fig. S5. Powder X-ray diffraction θ-2θ of $CeTaN_3$ ceramic target.

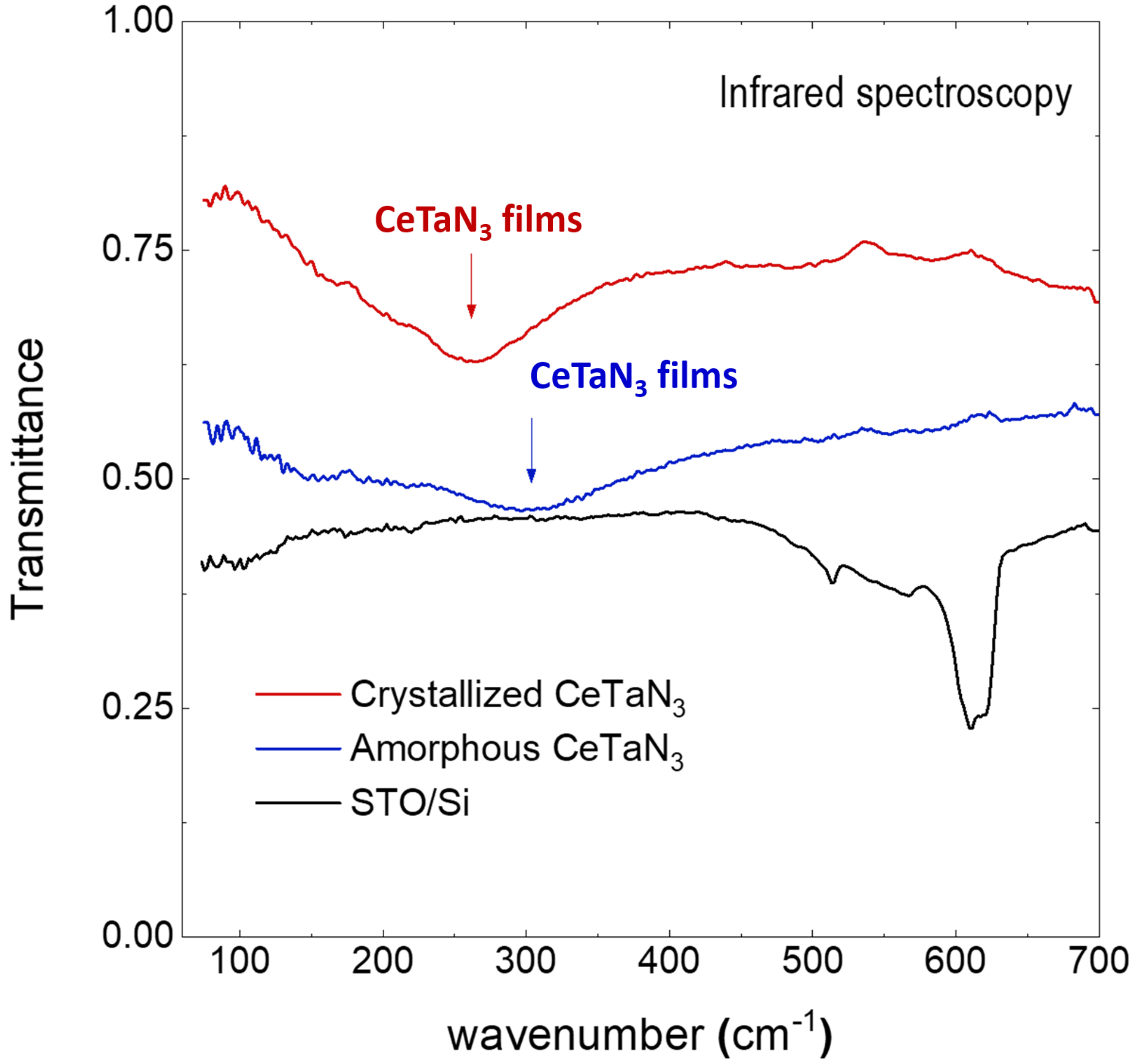

fig. S6. Infrared spectroscopy of crystalline $CeTaN_3$ with reference data from an amorphous $CeTaN_3$ and a $SrTiO_3$/Si substrate. Arrow lines mark the presence of $CeTaN_3$, in sharp difference with pure $SrTiO_3$/Si substrates.

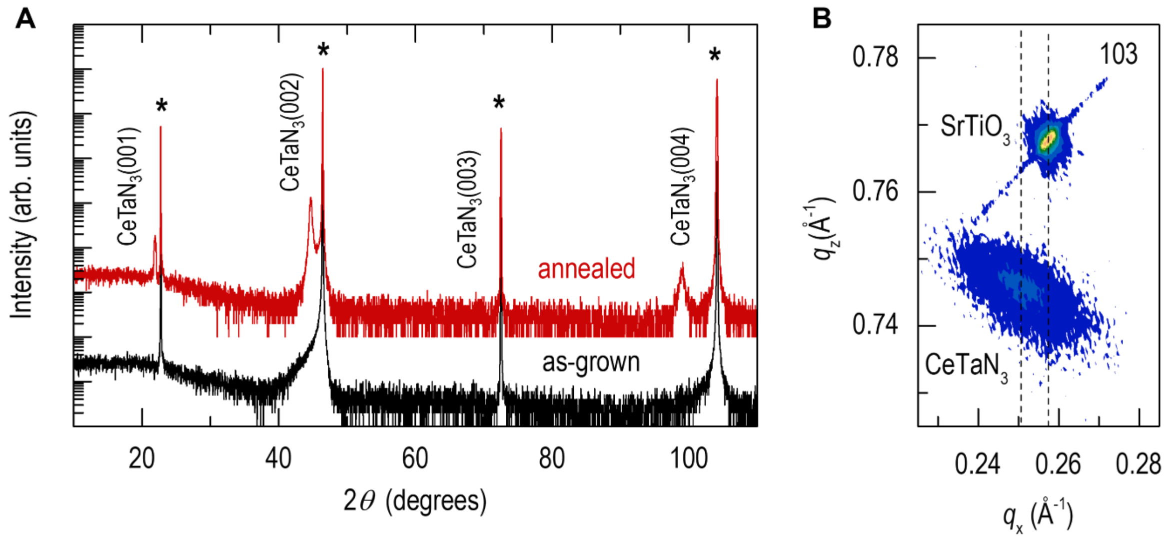

fig. S7. XRD measurements on amorphous and crystallized CeTaN$_3$ thin films on (001)-oriented SrTiO$_3$ substrates using rapid thermal process (RTP). (**A**) XRD θ-2θ scans of amorphous CeTaN$_3$ and crystalline CeTaN$_3$ before and after RTP, respectively. RTP was performed at the temperature of 800°C in ammonia (NH$_3$) conditions with 10,000 Pa for a 1 hour with heating rate of 200 °C/min. (**B**) RSM of CeTaN$_3$ around 103 peaks of SrTiO$_3$, yielding the in-plane and out-of-plane lattice constants of CTN films are 3.99 and 4.02 Å, respectively.

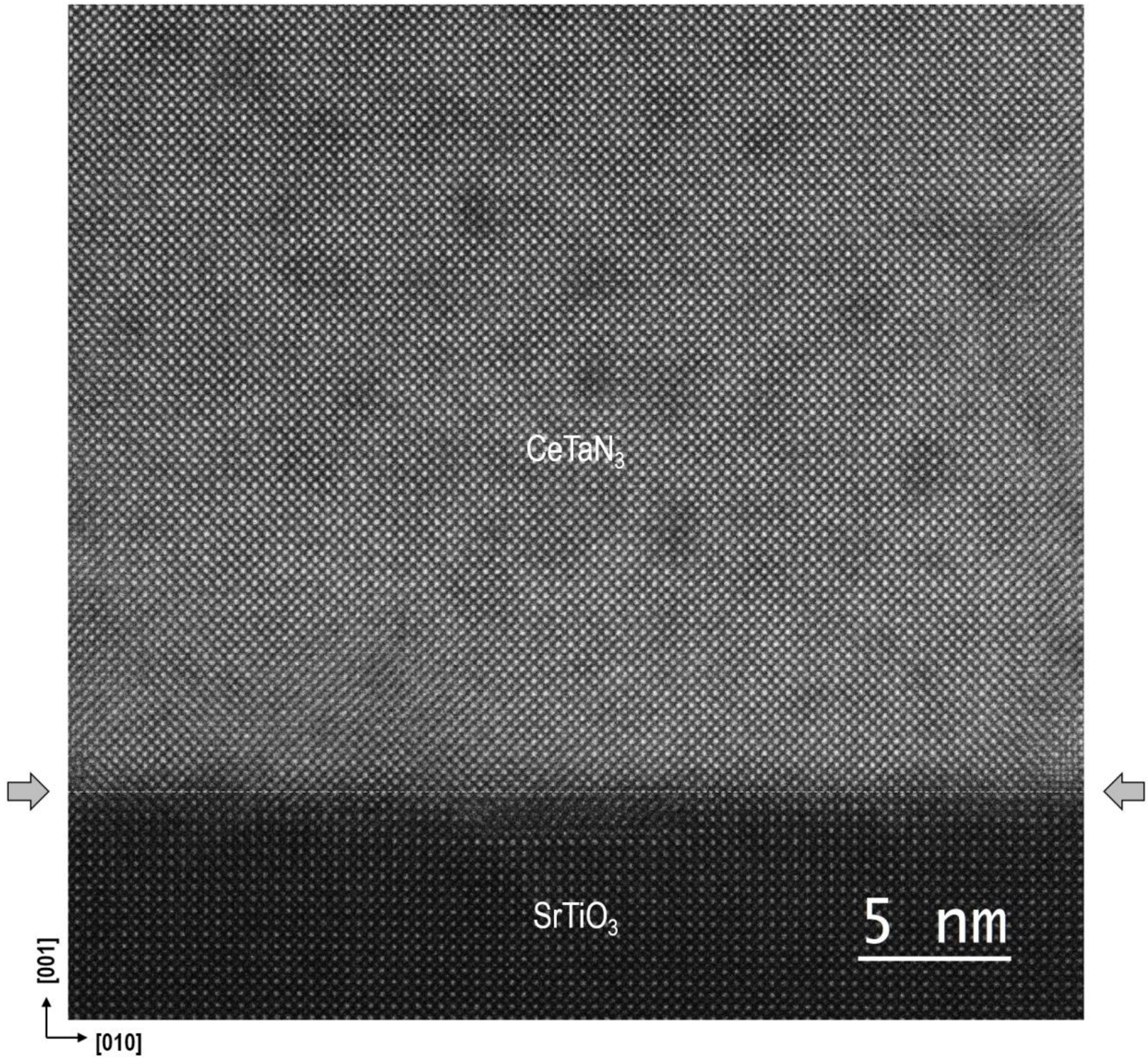

fig. S8. STEM-HAADF image of a $CeTaN_3$ thin film grown on $SrTiO_3$ substrates. Dashed line and arrows indicate the interfaces between $CeTaN_3$ and $SrTiO_3$. The sharp interfaces and well-ordered atoms indicate that the $CeTaN_3$ thin films have high crystallinity.

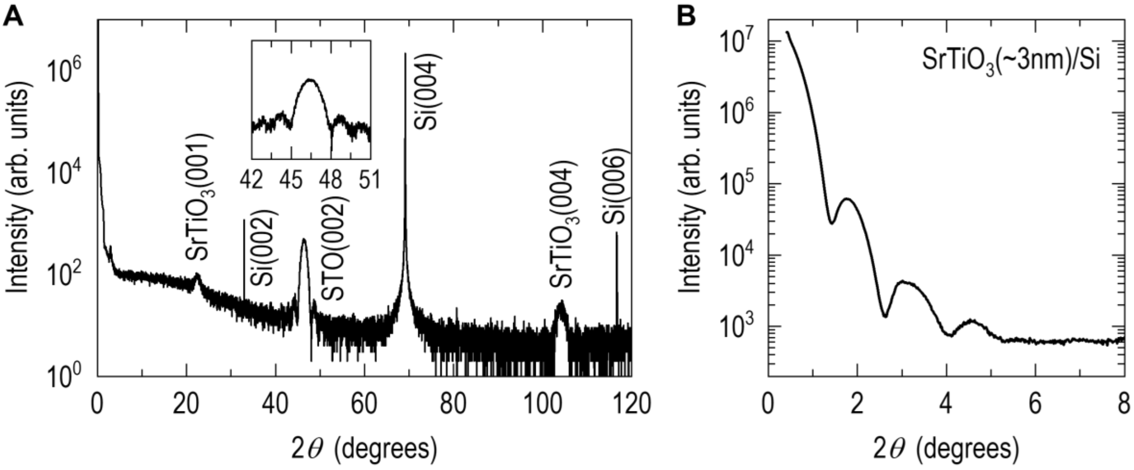

fig. S9. Structural characterization of 3 nm-thick STO capped Si substrate. (**A**) XRD θ-2θ scan exhibits the epitaxial growth of STO on Si without any impurity peaks. The inset shows the detail of the STO 002 peak, revealing the Kiessig fringes. (**B**) X-ray reflection (XRR) shows Fourier oscillations, confirming the flat surface and about 3nm thickness of the STO capping layer.

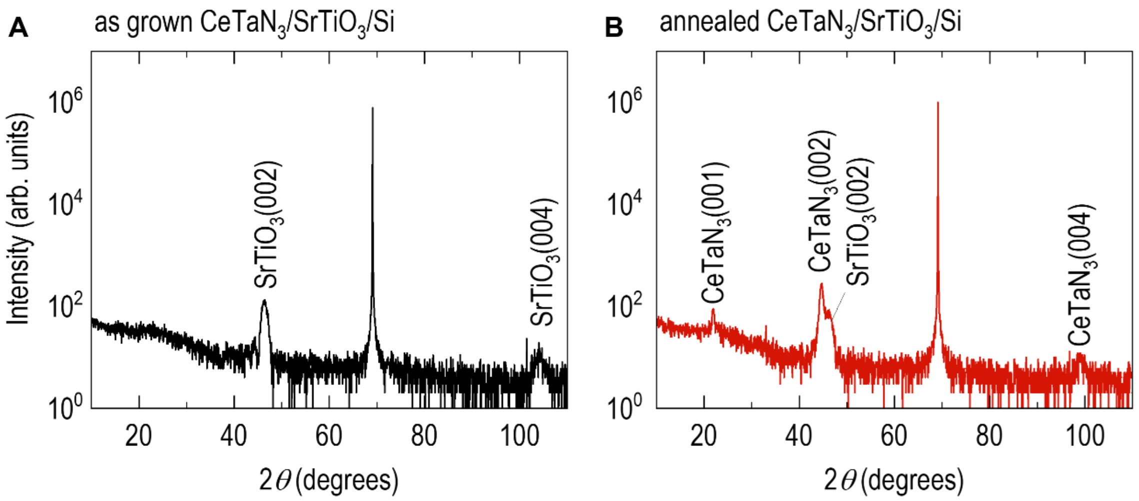

fig. S10. XRD θ-2θ of $CeTaN_3$ crystallization on STO/Si substrate using RTP. (**A**) Before RTP, XRD result only shows the STO peaks without any peaks from $CeTaN_3$ films, suggesting that the $CeTaN_3$ is amorphous. (**B**) We find the 00*l* reflections of $CeTaN_3$ films, indicating that the $CeTaN_3$ films are crystallized after RTP.

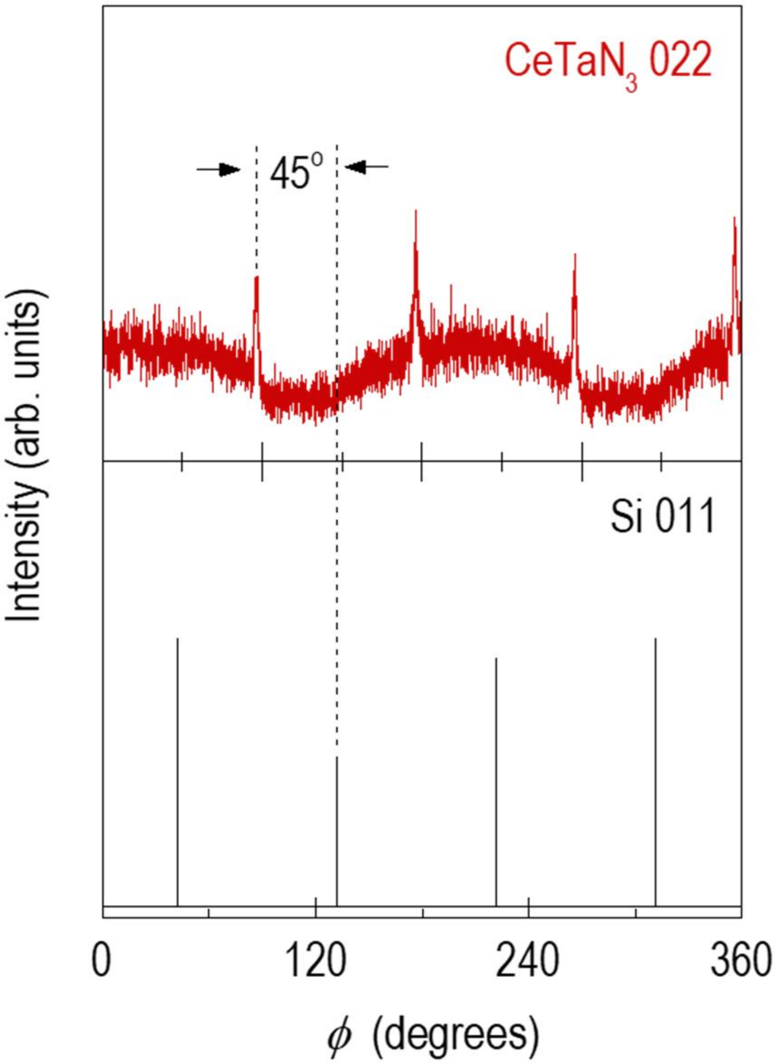

fig. S11. Phi-scans for CeTaN$_3$ 022 and Si 011 reflections. Two sets of curves shift by 45 degrees.

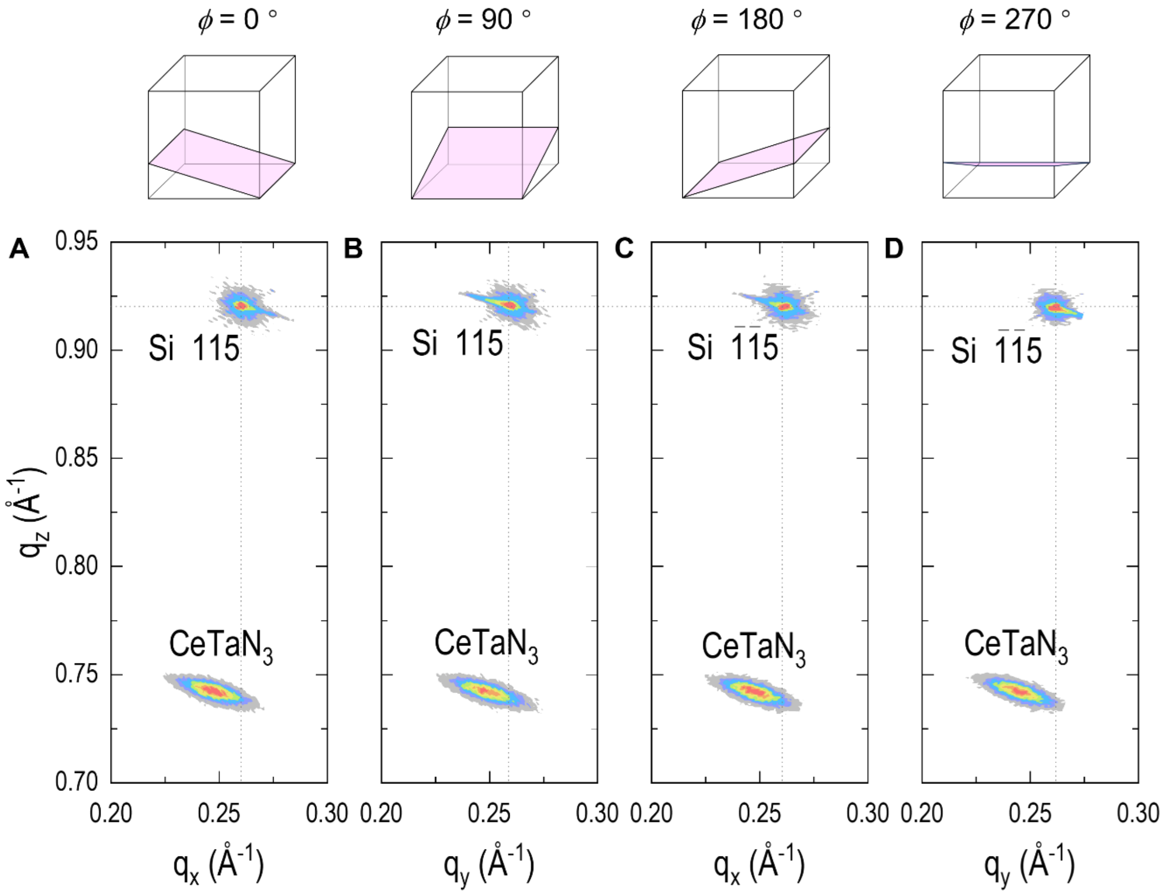

fig. S12. Tetragonal structure of $CeTaN_3$ thin films confirmed by RSM. The diffraction peaks, associated with the indices 103, 013, $\bar{1}03$, and $0\bar{1}3$ reflections of $CeTaN_3$, reveal consistent positioning of q_x and q_y. The phi-dependent RSM results suggest that the $CeTaN_3$ thin film exhibits a tetragonal structure. The average in-plane lattice parameter is calculated to be $a = b = 4.03$ Å, while the averaged out-of-plane lattice parameter is $c = 4.09$ Å.

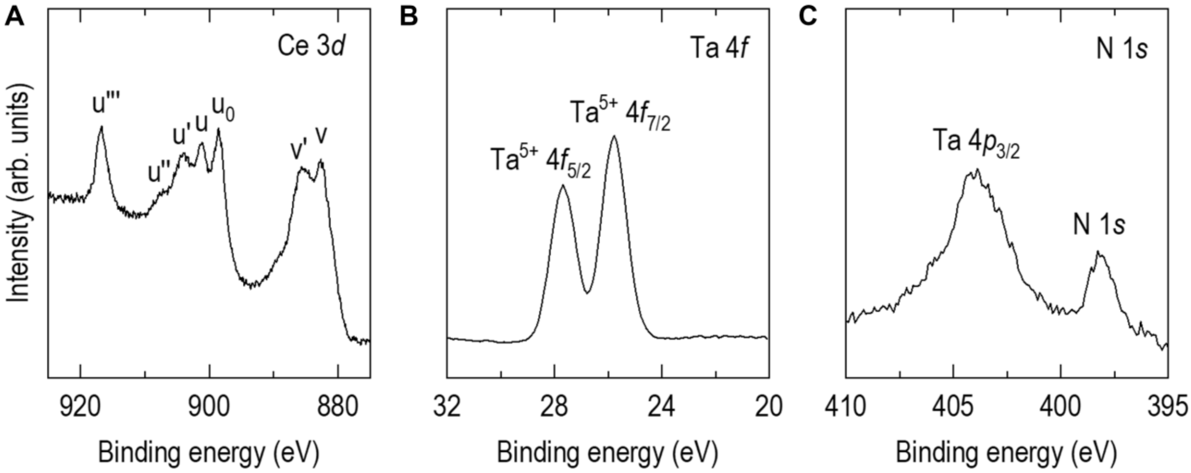

fig. S13. X-ray photoelectron spectroscopy of $CeTaN_3$ thin films. Ce 3*d*, Ta 4*d*, and N 1*s*, respectively. (**A**) Ce represents two oxidation states of Ce^{3+} and Ce^{4+}. The peaks of u' (901.3 eV), u_0 (898.5 eV), and v' (885.5 eV) correspond to the positions of Ce^{3+} determined from Ce_2O_3, while peaks of u''' (916.8 eV), u'' (907.2 eV), u (901.1 eV) and v (882.7 eV) match Ce^{4+} determined from CeO_2. The presence of two oxidization states may attribute to the inevitable nitrogen vacancies in the surface layers of $CeTaN_3$ thin films. (**B**) The result of Ta spectroscopy reveals a single oxidation state of Ta^{4+}. Ta^{5+} $4f_{5/2}$ is located at 27.7 eV, and Ta^{5+} $4f_{7/2}$ is at 25.8 eV. (**C**) N shows a distinct single peak at 398.1 eV, nearby where a peak corresponding to Ta $4p_{3/2}$ was observed at 403.9 eV.

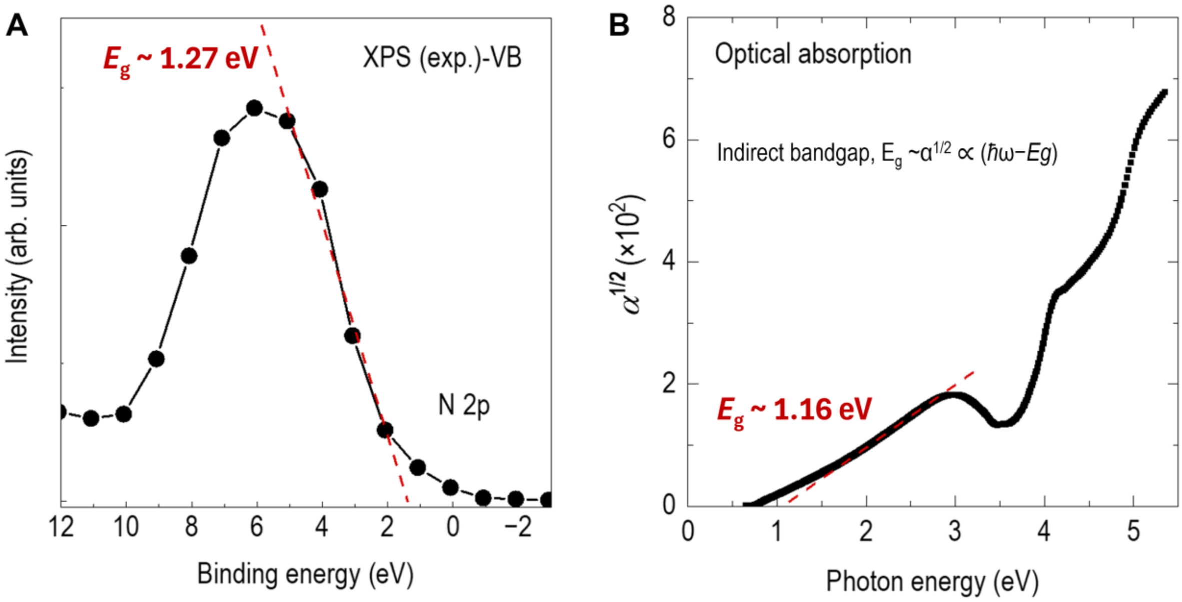

fig. S14. **Determination of band gap of $CeTaN_3$.** (**A**) XPS valence band (VB) spectra for $CeTaN_3$ thin films. The band gap estimated from VB spectra is approximately 1.27 eV. (**B**) Optical absorption spectra of a $CeTaN_3$ film on double-polished $SrTiO_3$ substrate. α represents the absorption coefficient. We plotted the $\alpha^{1/2}$ against the photon energy (*h*ω). The linear relationship between $\alpha^{1/2}$ and *h*ω demonstrates that the $CeTaN_3$ is an indirect band gap semiconductor, consistent with theoretical calculations. The optical band gap determined from absorption spectra is approximately 1.16 eV.

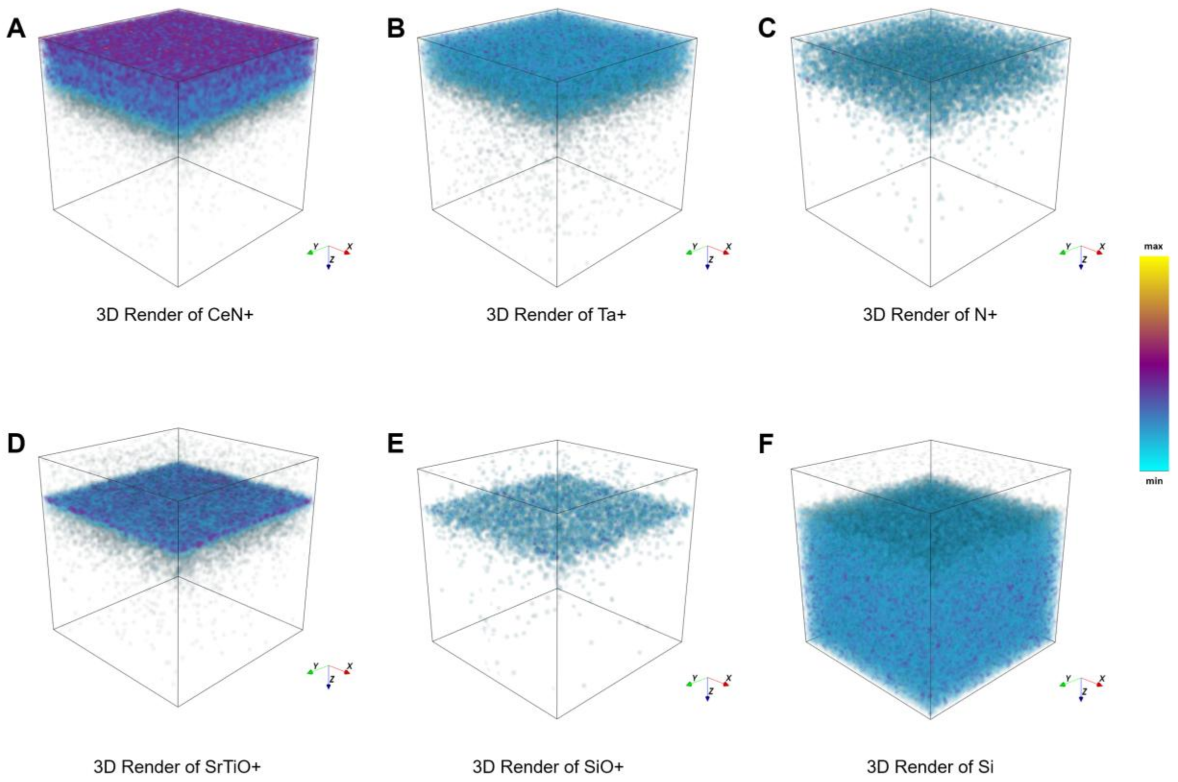

fig. S15. ToF-SIMS analysis of $CeTaN_3/SrTiO_3$/*a*-SiO_2/Si. (**A–F**) 3D renderings of CeN^+, Ta^+, N^+, $SrTiO^+$, SiO^+, and Si signals, respectively. The SIMS results confirm the uniformity of all deposited layers and provide insight into the chemical distribution from the top to the bottom of the structure.

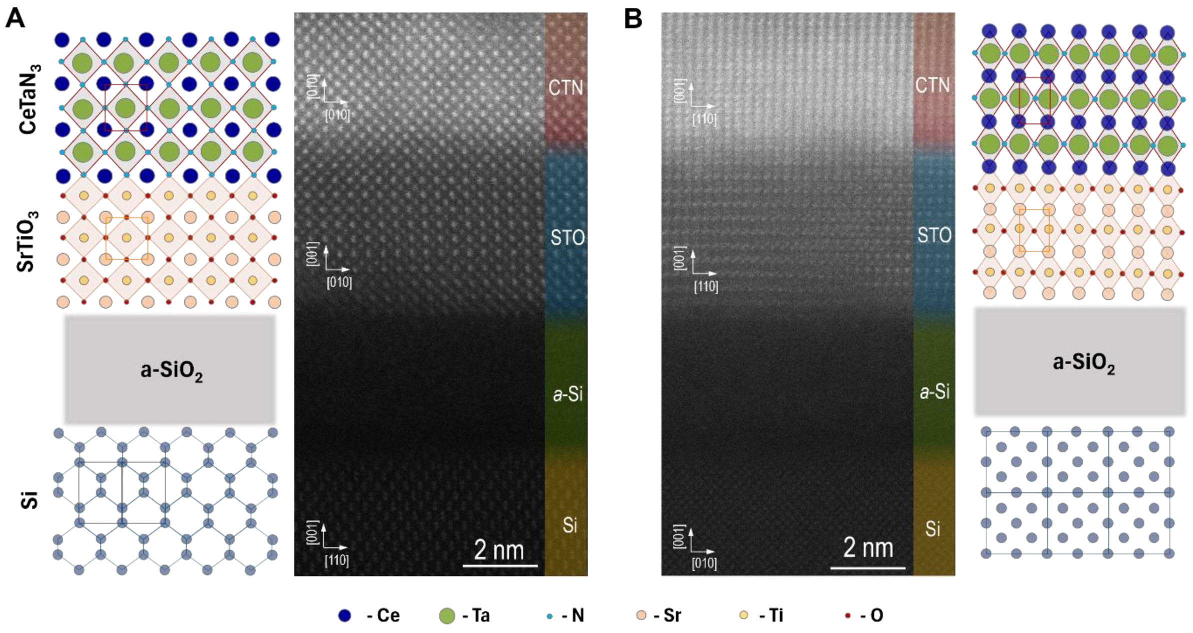

fig. S16. High resolution STEM images for a CeTaN$_3$/SrTiO$_3$/*a*-SiO$_2$/Si sample. (**A**) and (**B**) illustrate the STEM images viewed from Si [110] and Si [010] orientations, respectively.

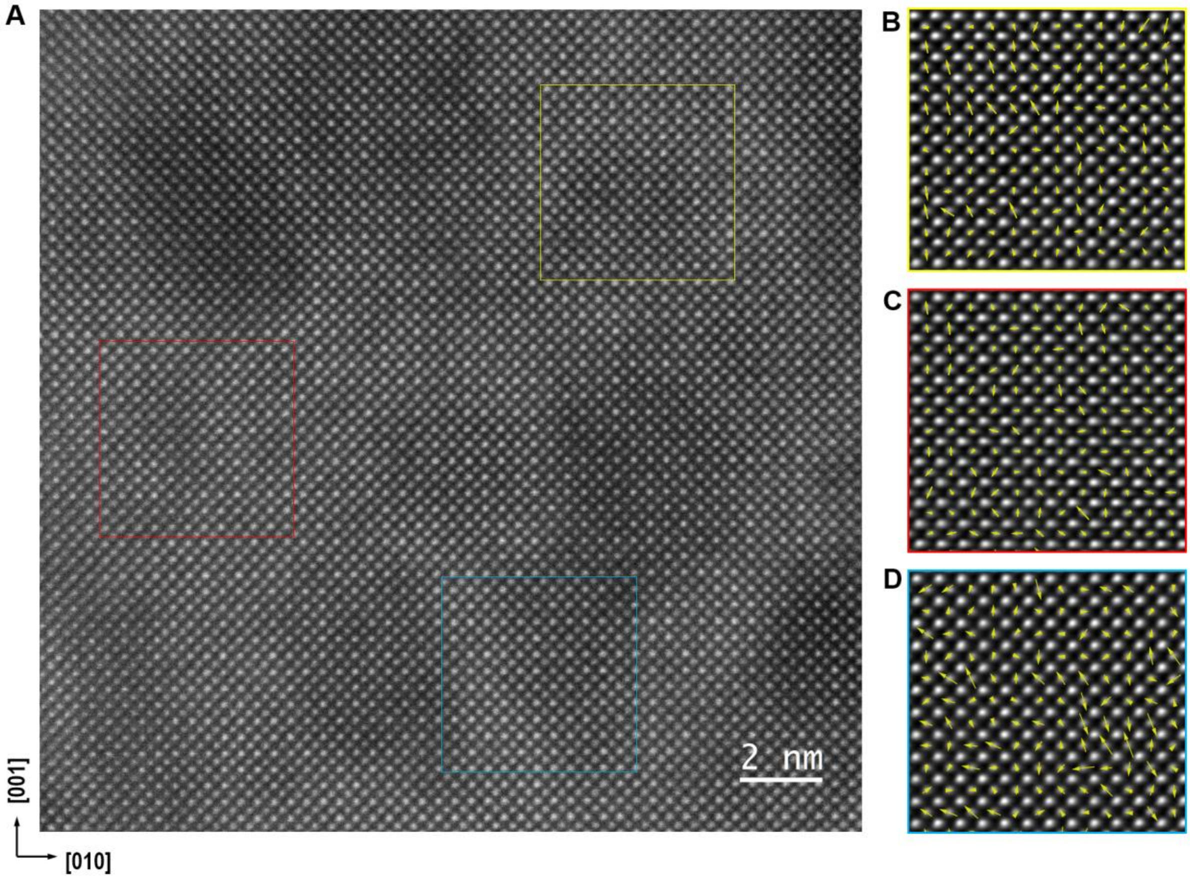

fig. S17. Polarization analysis of $CeTaN_3$. (**A**) A representative of zoom-in HAADF image of $CeTaN_3$. (**B** to **D**) The Ce atoms displacements were deduced from three representative TEM images. The arrows representing the motion of Ce atoms results to partial polarization, with most of these arrows pointing upward and some pointing to the left.

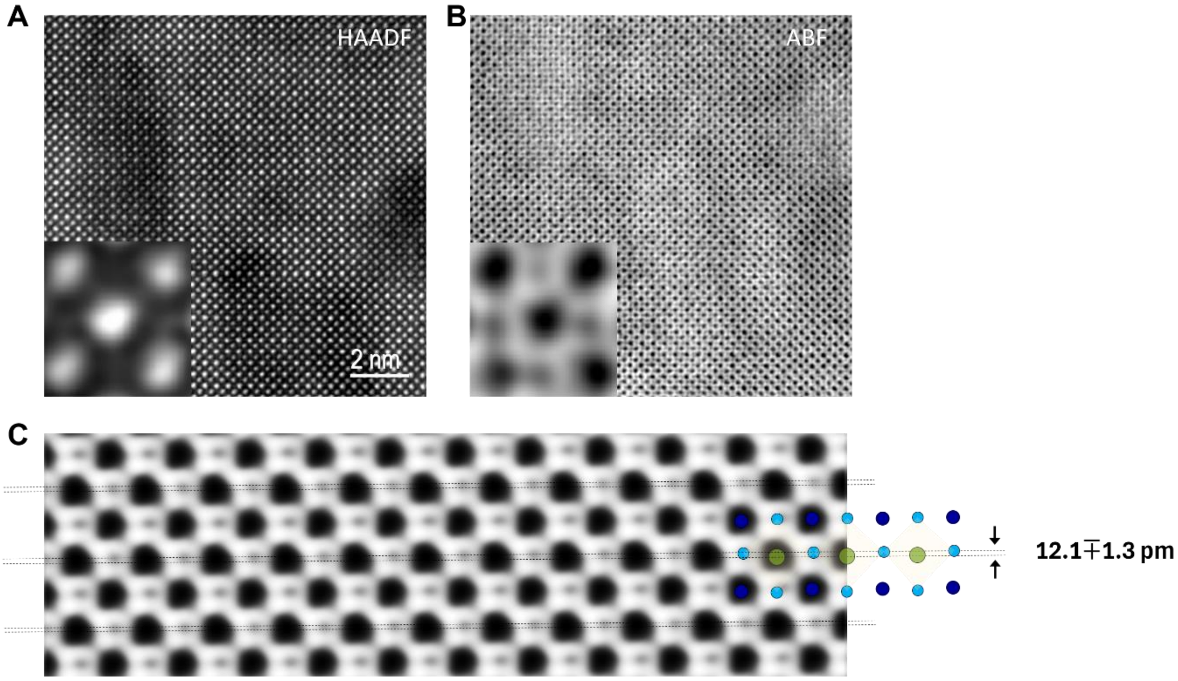

fig. S18. STEM results of CeTaN_3 thin films. To investigate atomic displacements intuitively related with ferroelectricity, **(A)** HAADF (high angle annular dark field) and **(B)** ABF (annular bright field) STEM images were recorded. **(C)** A ABF-STEM image of CeTaN_3, exhibiting schematic of non-centrosymmetric Ta atoms. The atomic displacement shifts from center position by 12.1 ± 1.3 pm.

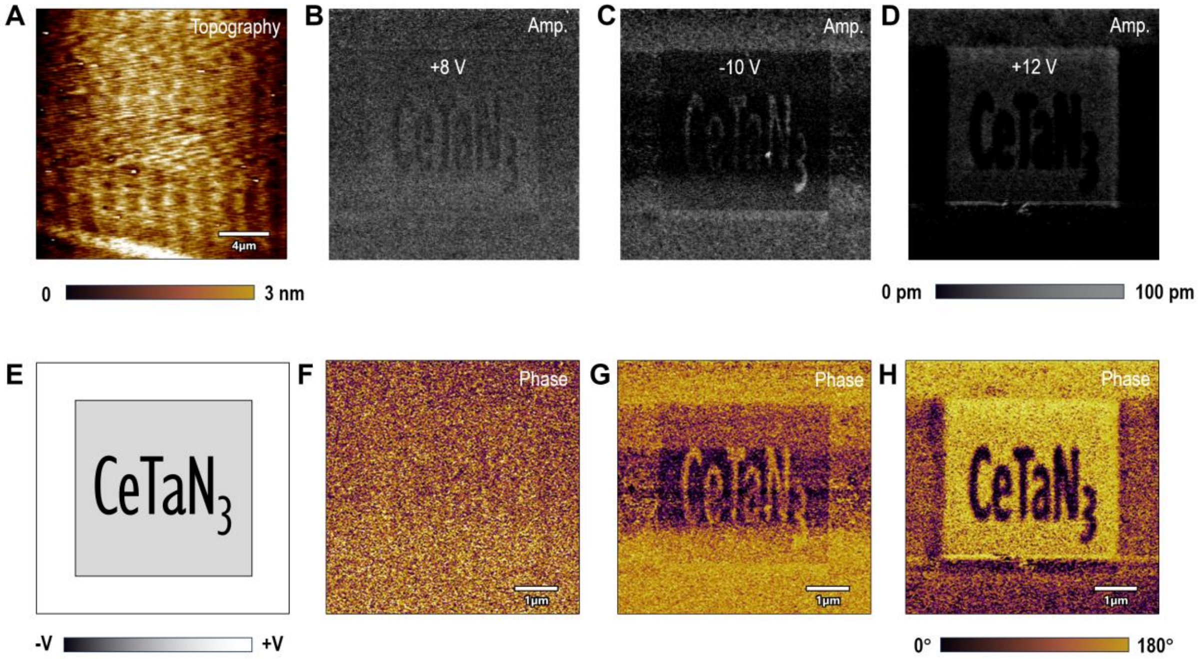

fig. S19. PFM results on a 15-nm-thick CeTaN$_3$ thin film grown on SrTiO$_3$/Si. (**A**) Topography of sample, yielding a r.m.s of ~ 2.7 nm. The “CeTaN$_3$” letters were written with opposite tip voltages comparing to the switching voltages poling the square area. (**B** to **D**) PFM amplitude and (**F** to **H**) PFM phase images with gradually increasing tip voltages. (**E**) Schematic of electrical switching patterns.

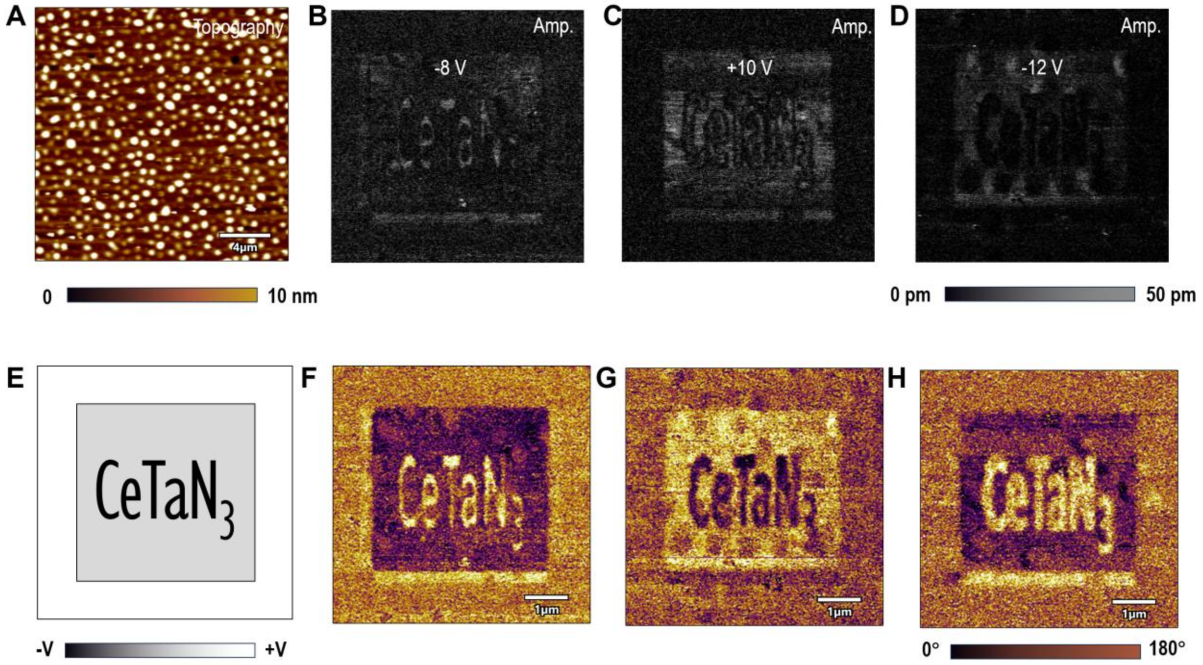

fig. S20. PFM results on an 80-nm-thick $CeTaN_3$ thin film grown on $SrTiO_3$/Si. (**A**) Topography of sample, yielding a r.m.s of ~ 8.3 nm. The "$CeTaN_3$" characters were written with opposite tip voltages comparing to the switching voltages poling the square area. (**B** to **D**) PFM amplitude and (**F** to **H**) PFM phase images with gradually increasing tip voltages. (**E**) Schematic of electrical switching patterns.

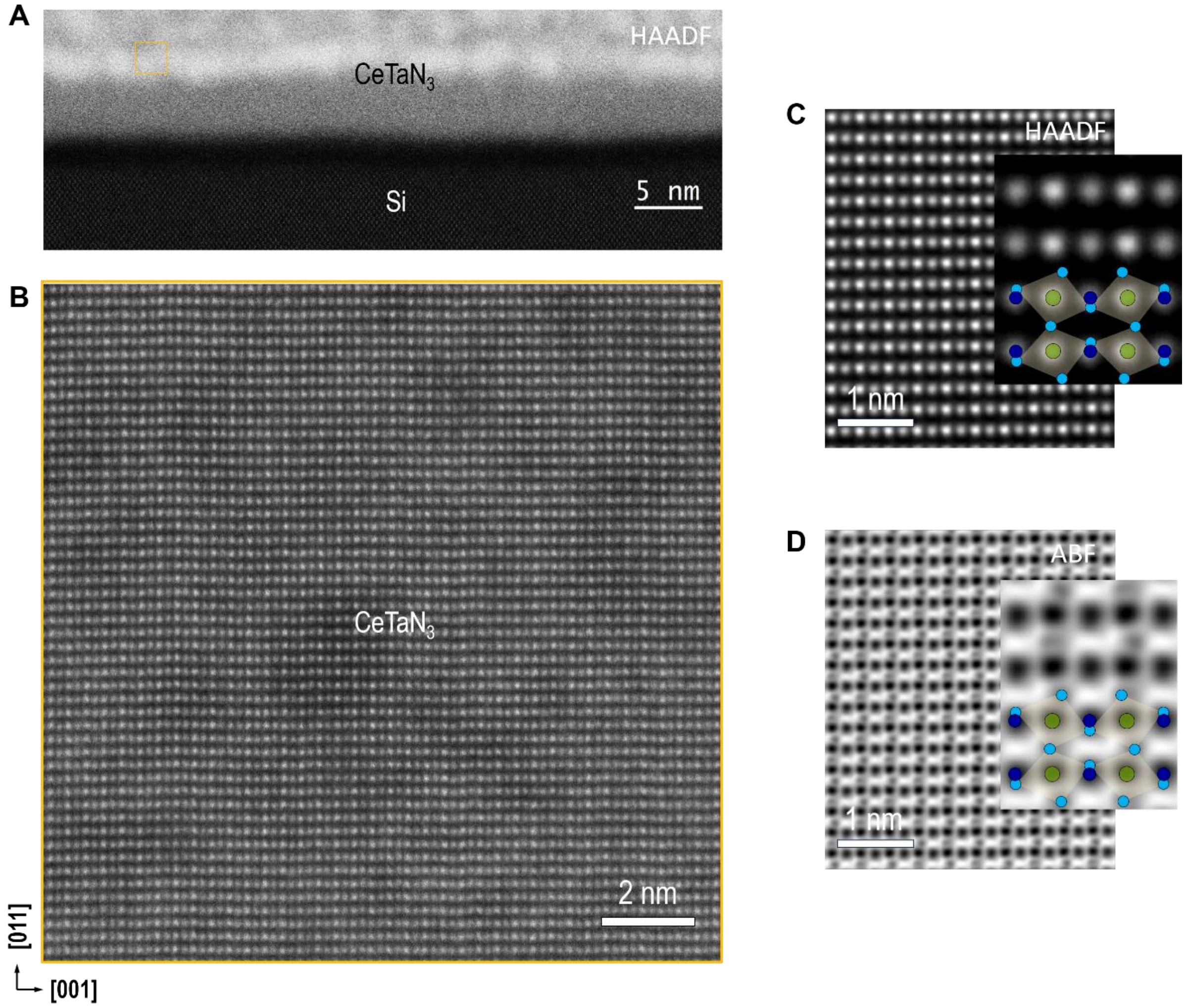

fig. S21. STEM analysis of $CeTaN_3$ thin films directly on Si. (**A**) Low magnification cross-sectional STEM-HAADF image at $CeTaN_3$/Si interfaces. Still, we cannot avoid the oxidization of Si at the interfaces at our growth conditions. The thickness of SiO_2 layer is approximately 1 nm. (**B**) High magnification STEM-HAADF image of $CeTaN_3$ thin films. The out-of-plane direction is along the [011] orientation. (**C**) STEM-HAADF and (**D**) STEM-ABF images of $CeTaN_3$, from which we could identify the tilted nitrogen octahedral.

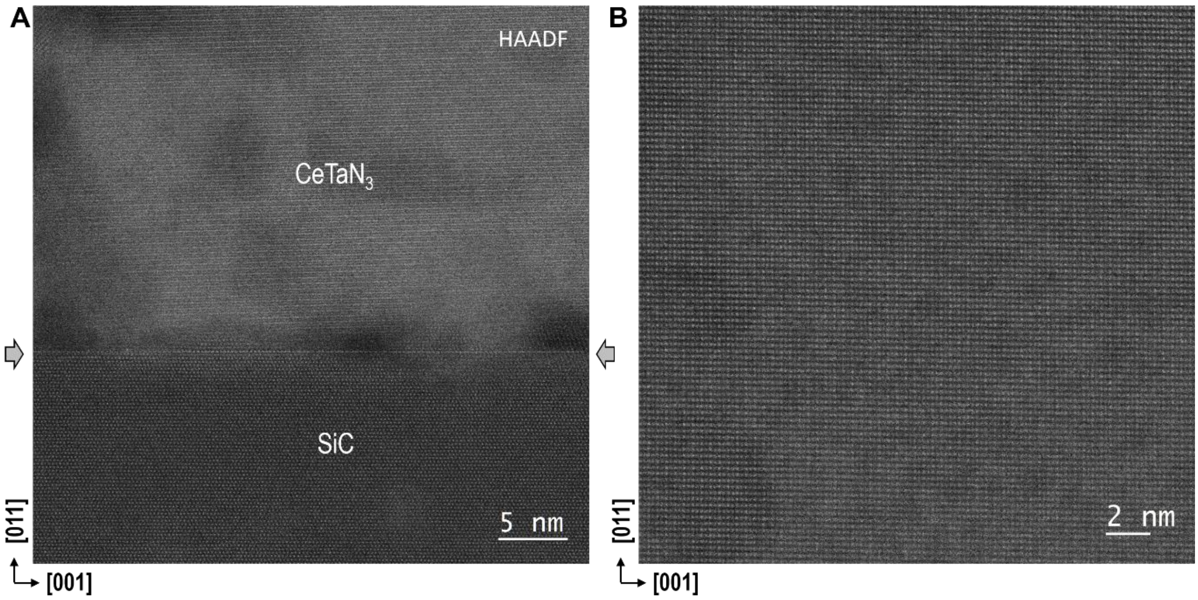

fig. S22. STEM analysis of CeTaN$_3$ thin films directly on SiC. (**A**) STEM-HAADF image at the CeTaN$_3$/SiC interface region. Arrows and dashed line indicate the position of interface. (**B**) High magnification STEM-HAADF image of CeTaN$_3$ thin films.

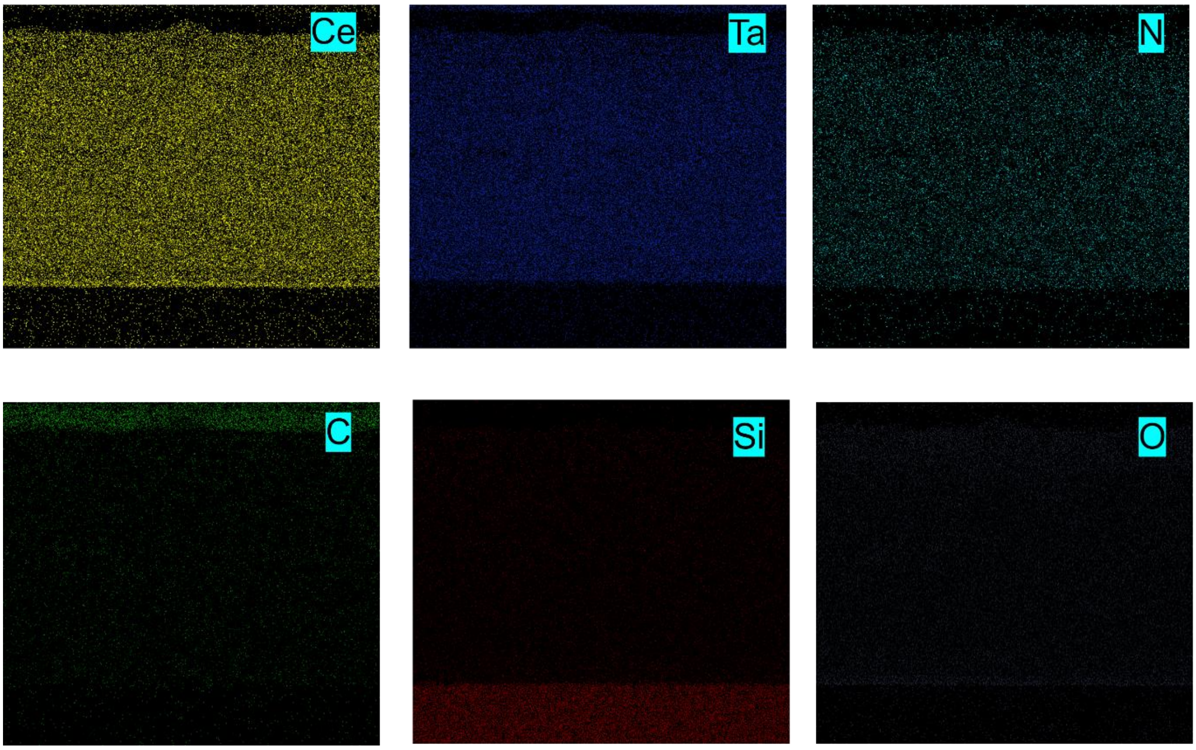

fig. S23. **Chemical distribution in $CeTaN_3$ thin films.** (**A** to **F**) EDX images of Ce, Ta, N, C, Si, and O elements. These results indicate that the $CeTaN_3$ films exhibit a high-crystallinity and chemical homogeneity without apparent contamination of oxygen.

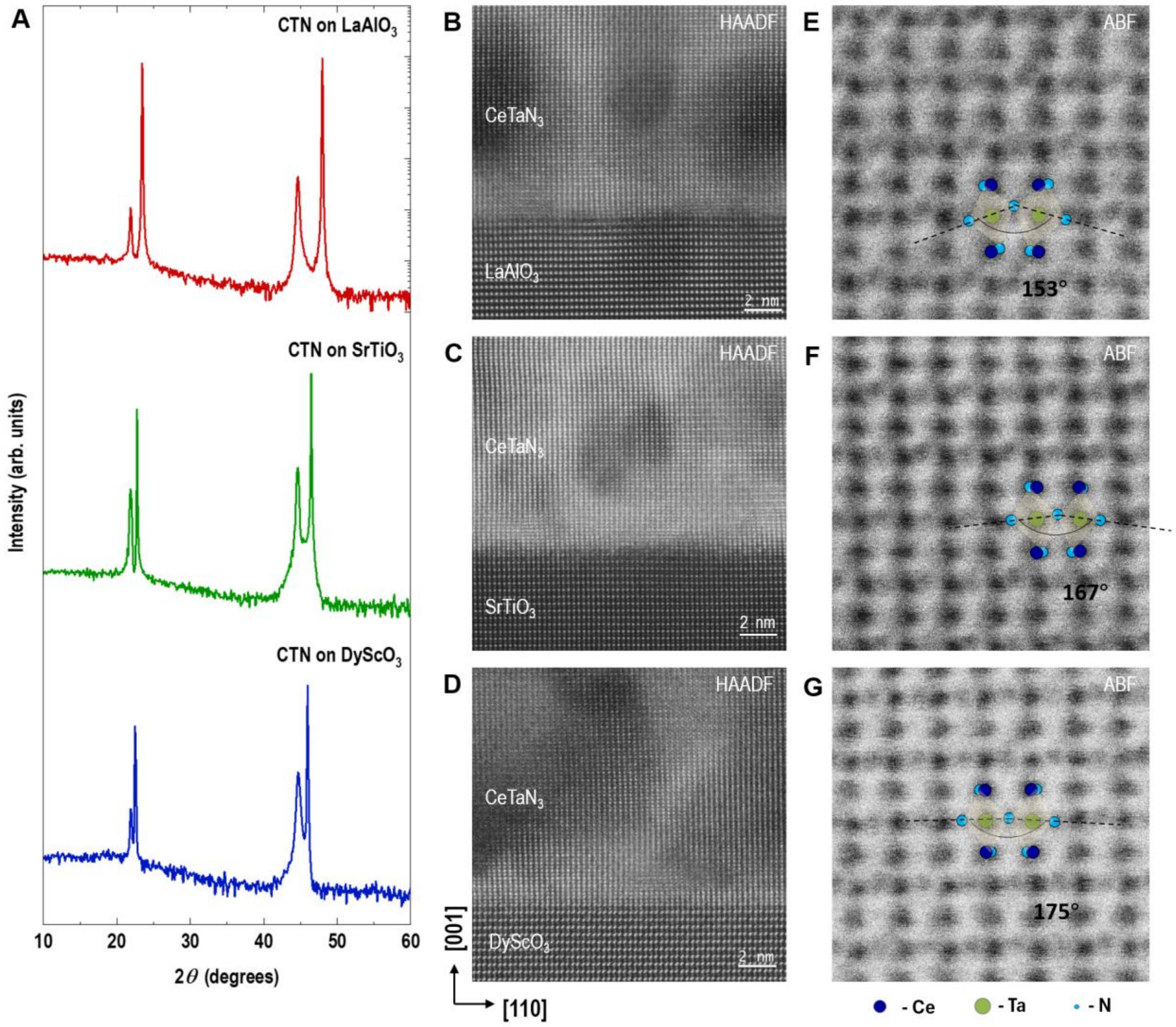

fig. S24. **Structural characterization of CeTaN$_3$ thin films on different oxide substrates.** (**A**) XRD θ-2θ scans of CeTaN$_3$ thin films grown on LaAlO$_3$, SrTiO$_3$, and DyScO$_3$ substrates, confirming their epitaxial growth. (**B–D**) HAADF-STEM images of CeTaN$_3$ thin films on LaAlO$_3$, SrTiO$_3$, and DyScO$_3$ substrates, respectively, revealing atomically sharp interfaces. (**E–G**) High-magnification ABF-STEM images of CeTaN$_3$ thin films on LaAlO$_3$, SrTiO$_3$, and DyScO$_3$ substrates, respectively. Insets in each ABF image illustrate the schematic of octahedral tilting, with the corresponding tilt angles indicated.

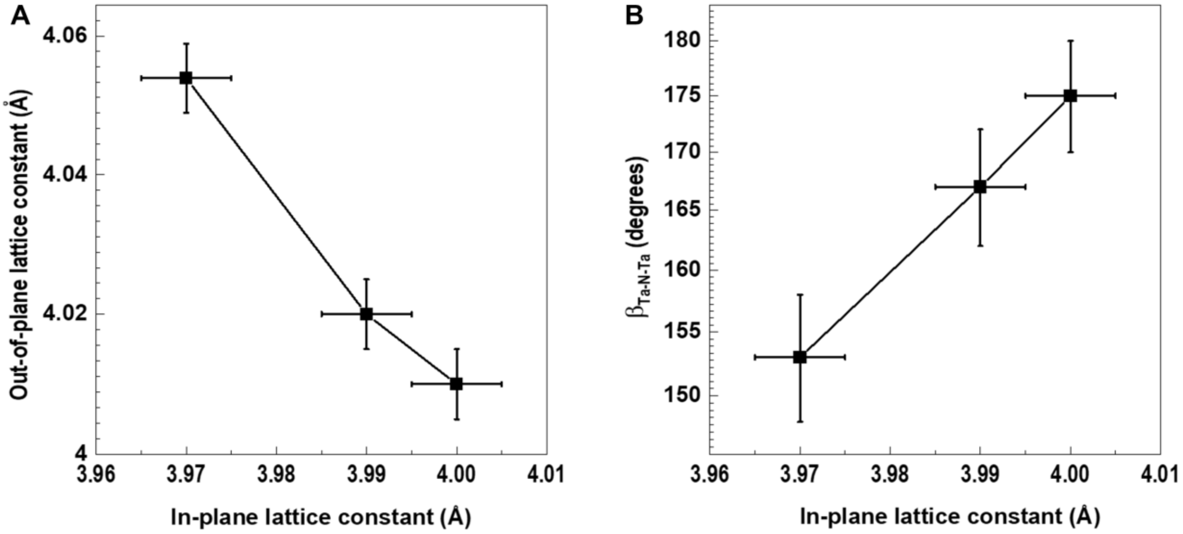

fig. S25. **Structural parameter evolution with in-plane lattice constant.** We determined the out-of-plane and in-plane lattice parameters of $CeTaN_3$ thin films using XRD measurements, including θ-2θ scans and reciprocal space mappings (RSMs). (**A**) Out-of-plane lattice parameters and (**B**) $\beta_{Ta–N–Ta}$ angle as a function of in-plane lattice constants for three $CeTaN_3$ thin films. The results clearly show that the $\beta_{Ta–N–Ta}$ angle progressively decreases with increasing compressive strain, following the trend from $DyScO_3$ to $SrTiO_3$ and $LaAlO_3$ substrates.

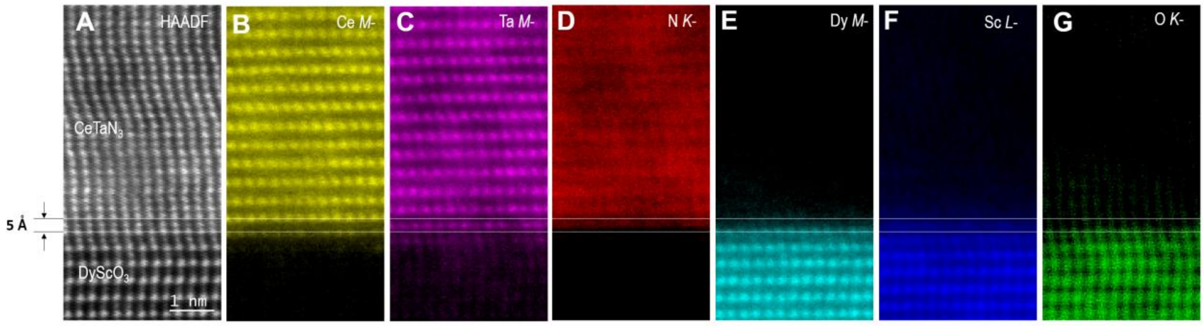

fig. S26. **EELS mapping of $CeTaN_3$ thin films on $DyScO_3$ substrates.** (**A**) HAADF-STEM image, where the tilt is attributed to thermal drift during STEM imaging. (**B–G**) Atomically resolved EELS maps corresponding to the Ce *M*-, Ta *M*-, N *K*-, Dy *M*-, Sc *L*-, and O *K*-edges. These results confirm the exceptionally high chemical homogeneity of $CeTaN_3$ thin films, with minimal chemical intermixing at the heterointerface, limited to a length scale of one unit cell. The interface termination is identified as TaN_2–DyO.

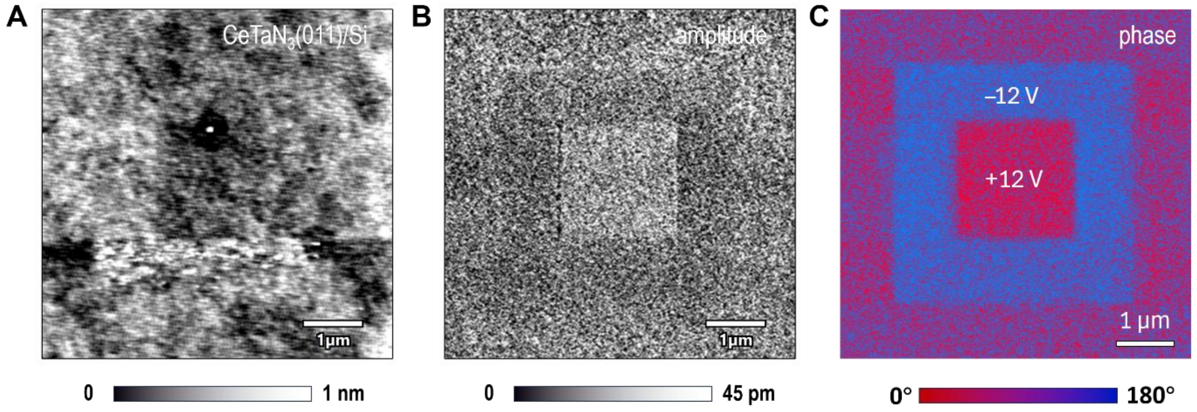

fig. S27. PFM results of CeTaN$_3$ thin films directly grown on Si. (**A**) Topography of CeTaN$_3$/Si. The r.m.s of sample is ~ 1 nm. (**B**) PFM amplitude and (**C**) phase images of CeTaN$_3$/Si. The center and border square area was upward and downward polarized by tip voltages, respectively. the square shapes show reversal phase and amplitude of piezoelectric responses.

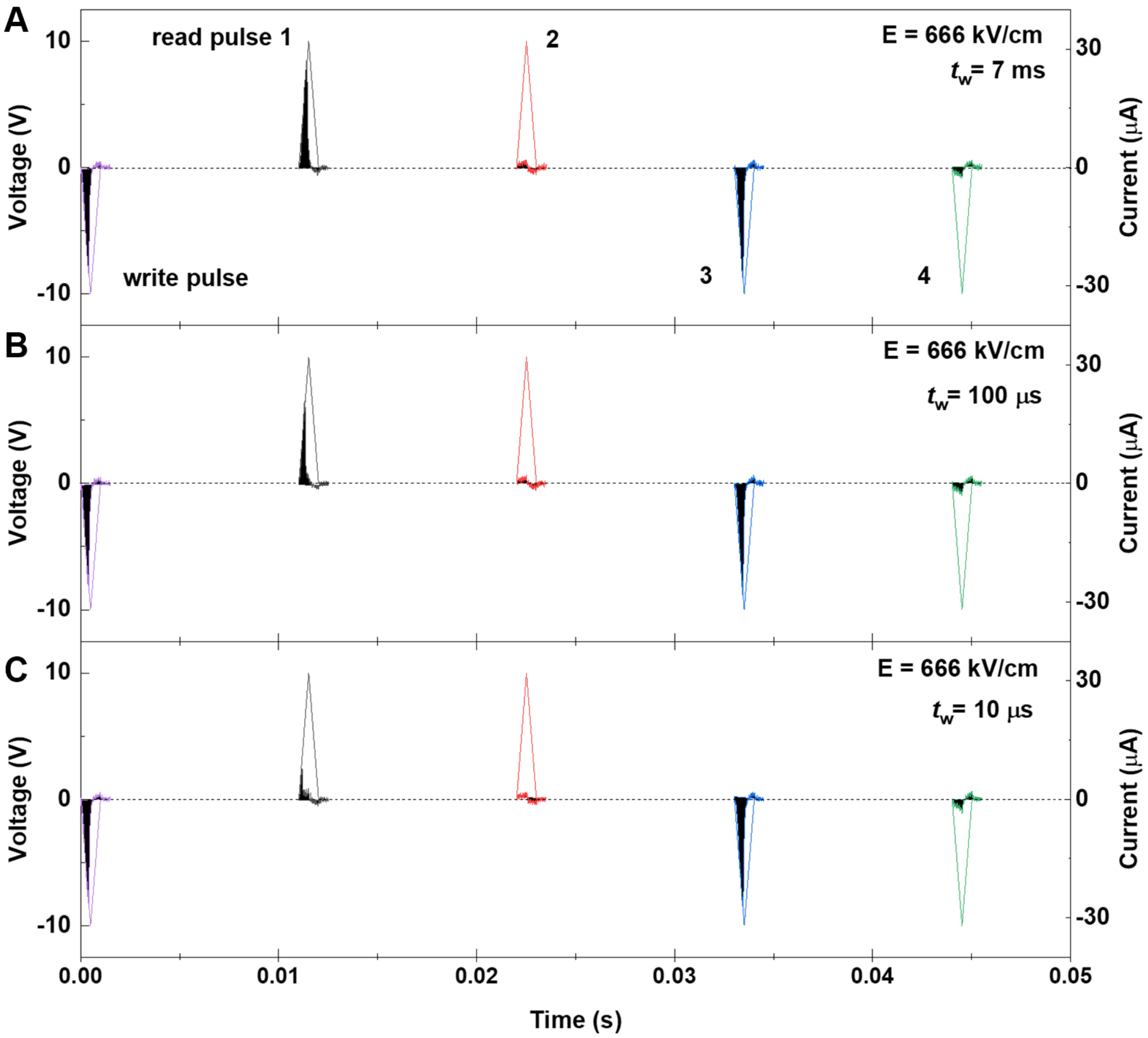

fig. S28. **PUND measurements on a Pt/CeTaN$_3$/*p*-Si capacitor.** (**A–C**) PUND measurements were conducted with a fixed poling electric field (V_w = 10 V, corresponding to 667 kV/cm) at different writing times (t_w = 7 ms, 100 µs, and 10 µs), respectively. A sharp difference is observed in the read pulse 1, revealing distinct switching currents.

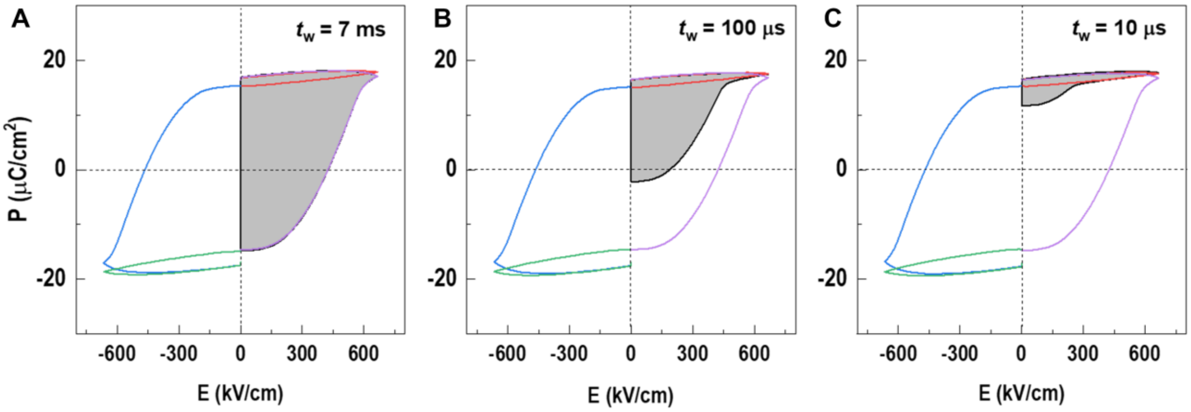

fig. S29. **Ferroelectric hysteresis loops of Pt/CeTaN$_3$/*p*-Si capacitor under different writing times (t_w).** These results are calculated from Fig. S27 A-C. The write and read curves correspond to the curves described in Fig. S27. The shadow areas represent the switched ferroelectric polarizations under different t_w.

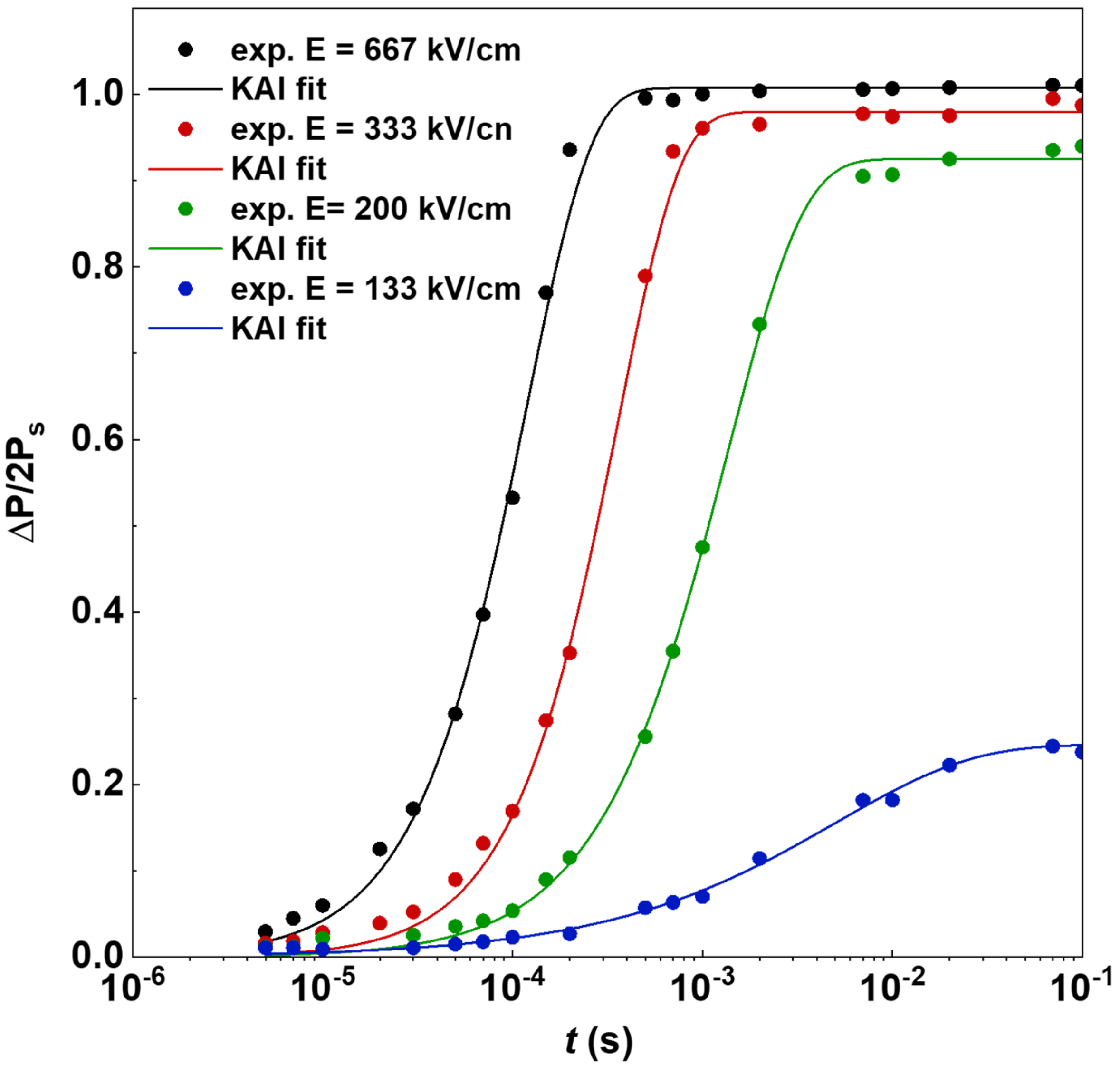

fig. S30. **Ferroelectric switching tests on a Pt/$CeTaN_3$/*p*-Si capacitor.** The switched polarization (ΔP) as a function of *t* for four different electric fields. ΔP were obtained by varying the pulse duration (*t*) while keeping the electric field constant. According to the Kolmogorov-Avrami-Ishibashi (KAI) model (*58, 59*), the switched polarization follows the relation $\Delta P = 2P_s\{1 - \exp\left[-t/t_{sw}\right]\}$ for a continuous one-dimensional medium. Fitting the data using the KAI model reveals that the switching time ranges from 1.18×10^{-4} s to 0.005 s, depending on the poling fields. Higher electric fields result in faster ferroelectric domain switching.

REFERENCES AND NOTES

1. R. A. McKee, F. J. Walker, M. F. Chisholm, Crystalline oxides on silicon: The first five monolayers. *Phys. Rev. Lett.* **81**, 3014–3017 (1998).

2. A. Pasquarello, M. S. Hybertsen, R. Car, Interface structure between silicon and its oxide by first-principles molecular dynamics. *Nature* **396**, 58–60 (1998).

3. M. P. Warusawithana, C. Cen, C. R. Sleasman, J. C. Woicik, Y. Li, L. F. Kourkoutis, J. A. Klug, H. Li, P. Ryan, L.-P. Wang, M. Bedzyk, D. A. Muller, L.-Q. Chen, J. Levy, D. G. Schlom, A ferroelectric oxide made directly on silicon. *Science* **324**, 367–370 (2009).

4. S. H. Baek, J. Park, D. M. Kim, V. A. Aksyuk, R. R. Das, S. D. Bu, D. A. Felker, J. Lettieri, V. Vaithyanathan, S. S. N. Bharadwaja, N. Bassiri-Gharb, Y. B. Chen, H. P. Sun, C. M. Folkman, H. W. Jang, D. J. Kreft, S. K. Streiffer, R. Ramesh, X. Q. Pan, S. Trolier-McKinstry, D. G. Schlom, M. S. Rzchowski, R. H. Blick, C. B. Eom, Giant piezoelectricity on Si for hyperactive MEMS. *Science* **334**, 958–961 (2011).

5. S. K. Lee, B. H. Choi, D. Hesse, Epitaxial growth of multiferroic $BiFeO_3$ thin films with (101) and (111) orientations on (100) Si substrates. Epitaxial growth of multiferroic $BiFeO_3$ thin films with (101) and (111) orientations on (100) Si substrates. *Appl. Phys. Lett.* **102**, 242906 (2013).

6. M. Suzuki, Review on future ferroelectric nonvolatile memory: FeRAM. *J. Cerma. Soc. Jpn.* **103**, 1099–1111 (1995).

7. P. Vettiger, G. Binnig, The Nanodrive Project. *Sci. Am.* **288**, 46 (2003).

8. A. L. Esaki, R. B. Laibowitz, P. J. Stiles, Polar switch. *IBM Tech. Discl. Bull* **13**, 2161 (1971).

9. Y.-R. Wu, J. Singh, Polar heterostructure for multifunction devices: Theoretical studies. *IEEE Trans. Electron Devives* **52**, 284–293 (2005).

10. S. S. Cheema, D. Kwon, N. Shanker, R. dos Reis, S.-L. Hsu, J. Xiao, H. Zhang, R. Wagner, A. Datar, M. R. McCarter, C. R. Serrao, A. K. Yadav, G. Karbasian, C.-H. Hsu, A. J. Tan, L.-C. Wang, V. Thakare, X. Zhang, A. Mehta, E. Karapetrova, R. V. Chopdekar, P. Shafer, E. Arenholz, C. Hu, R. Proksch, R. Ramesh, J. Ciston, S. Salahuddin, Enhanced ferroelectricity in ultrathin films grown directly on silicon. *Nature* **580**, 478–482 (2020).

11. S. S. Cheema, N. Shanker, L.-C. Wang, C.-H. Hsu, S.-L. Hsu, Y.-H. Liao, M. S. Jose, J. Gomez, W. Chakraborty, W. Li, J.-H. Bae, S. K. Volkman, D. Kwon, Y. Rho, G. Pinelli, R. Rastogi, D. Pipitone, C. Stull, M. Cook, B. Tyrrell, V. A. Stoica, Z. Zhang, J. W. Freeland, C. J. Tassone, A. Mehta, G. Saheli, D. Thompson, D. I. Suh, W.-T. Koo, K.-J. Nam, D. J. Jung, W.-B. Song, C.-H. Lin, S. Nam, J. Heo, N. Parihar, C. P. Grigoropoulos, P. Shafer, P. Fay, R. Ramesh, S. Mahapatra, J. Ciston, S. Datta, M. Mohamed, C. Hu, S. Salahuddin, Ultrathin ferroic HfO_2-ZrO_2 superlattice gate stack for advanced transistors. *Nature* **604**, 65–71 (2022).

12. S. S. Cheema, N. Shanker, S.-L. Hsu, Y. Rho, C.-H. Hsu, V. A. Stoica, Z. Zhang, J. W. Freeland, P. Shafer, C. P. Grigoropoulos, J. Ciston, S. Salahuddin, Emergent ferroelectricity in subnanometer binary oxide films on silicon. *Science* **376**, 648–652 (2022).

13. K. J. Hubbard, D. G. Schlom, Thermodynamic stability of binary oxides in contact with silicon. *J. Mater. Res.* **11**, 2757–2776 (1996).

14. N. E. Brese, F. J. DiSalvo, Synthesis of the first thorium-containing nitride perovskite, $TaThN_3$. *J. Solid State Chem.* **120**, 378–380 (1995).

15. R. Sarmiento-Pérez, T. F. T. Cerqueira, S. Körbel, S. Botti, M. A. L. Marques, Prediction of stable nitride perovskites. *Chem. Mater.* **27**, 5957–5963 (2015).

16. Y.-W. Fang, C. A. J. Fisher, A. Kuwabara, X.-W. Shen, T. Ogawa, H. Moriwake, R. Huang, C.-G. Duan, Lattice dynamics and ferroelectric properties of the nitride perovskite $LaWN_3$. *Phys. Rev. B* **95**, 014111 (2017).

17. C. Gui, J. Chen, S. Dong, Multiferroic nitride perovskites with giant polarizations and large magnetic moments. *Phys. Rev. B* **106**, 184418 (2022).

18. X. Zi, Z. Deng, L. Rao, Y. Li, G. Tang, J. Hong, J., First-principles study of ferroelectric, dielectric, and piezoelectric properties in the nitride perovskites Ce BN_3(B = Nb, Ta). *Phys. Rev. B* **109**, 115125 (2024).

19. K. R. Talley, C. L. Perkins, D. R. Diercks, G. L. Brennecka, A. Zakutayev, A., Synthesis of $LaWN_3$ nitride perovskite with polar symmetry. *Science* **374**, 1488–1491 (2021).

20. V.-A. Ha, H. Lee, F. Giustino, $CeTaN_3$ and $CeNbN_3$: Prospective nitride perovskites with optimal photovoltaic band gaps. *Chem. Mater.* **34**, 2107–2122 (2022).

21. R. Sherbondy, R. W. Smaha, C. J. Bartel, M. E. Holtz, K. R. Talley, B. Levy-Wendt, C. L. Perkins, S. Eley, A. Zakutayev, G. L. Brennecka, High-throughput selection and experimental realization of two new Ce-based nitride perovskites: $CeMoN_3$ and $CeWN_3$. *Chem. Mater.* **34**, 6883–6893 (2022).

22. A. Biswas, C.-H. Yang, R. Ramesh, Y. H. Jeong, Atomically flat single terminated oxide substrate surfaces. *Prog. Surf. Sci.* **92**, 117–141 (2017).

23. X. Zhou, W. Xu, Z. Gui, C. Gu, J. Chen, J. Xie, X. Yao, J. Dai, J. Zhu, L. Wu, E.-j. Guo, X. Yu, L. Fang, Y. Zhao, L. Huang, S. Wang, Polar nitride perovskite $LaWN_{3-\delta}$ with orthorhombic structure. *Adv. Sci.* **10**, 2205479 (2023).

24. P. Gao, C. T. Nelson, J. R. Jokisaari, S. H. Baek, C. W. Bark, Y. Zhang, E. Wang, D. G. Schlom, C. B. Eom, X. Pan, Revealing the role of defects in ferroelectric switching with atomic resolution. *Nat. Commun.* **2**, 591 (2011).

25. E.-J. Guo, R. Roth, A. Herklotz, D. Hesse, K. Dörr, K., Ferroelectric 180° domain wall motion controlled by biaxial strain. *Adv. Mater.* **27**, 1615–1618 (2015).

26. S. Geng, Z. Xiao, Can nitride perovskites provide the same superior optoelectronic properties as lead halide perovskites? *ACS Energy Lett.* **8**, 2051–2057 (2023).

27. E. Aydin, T. G. Allen, M. D. Bastiani, A. Razzaq, L. Xu, E. Ugur, J. Liu, S. D. Wolf, Pathways toward commercial perovskite/silicon tandem photovoltaics. *Science* **383**, 6679 (2024).

28. B. F. Grosso, D. W. Davies, B. Zhu, A. Walsh, D. O. Scanlon, Accessible chemical space for metal nitride perovskites. *Chem. Sci.* **14**, 9175–9185 (2023).

29. Q. Jin, H. Cheng, Z. Wang, Q. Zhang, S. Lin, M. A. Roldan, J. Zhao, J.-O. Wang, S. Chen, M. He, C. Ge, C. Wang, H.-B. Lu, H. Guo, L. Gu, X. Tong, T. Zhu, S. Wang, H. Yang, K.-j. Jin, E.-J. Guo, Strain-mediated high conductivity in ultrathin antiferromagnetic metallic nitrides. *Adv. Mater.* **33**, e2005920 (2021).

30. Q. Jin, Z. Wang, Q. Zhang, Y. Yu, S. Lin, S. Chen, M. Qi, H. Bai, A. Huon, Q. Li, L. Wang, X. Yin, C. S. Tang, A. T. S. Wee, F. Meng, J. Zhao, J.-o. Wang, H. Guo, C. Ge, C. Wang, W. Yan, T. Zhu, L. Gu, S. A. Chambers, S. Das, T. Charlton, M. R. Fitzsimmons, G.-Q. Liu, S. Wang, K.-j. Jin, H. Yang, E.-J. Guo, Room-temperature ferromagnetism at an oxide-nitride interface. *Phys. Rev. Lett.* **128**, 017202 (2022).

31. Q. Jin, Q. Zhang, H. Bai, M. Yang, Y. Ga, S. Chen, H. Hong, T. Cui, D. Rong, T. Lin, J.-O. Wang, C. Ge, C. Wang, Y. Cao, L. Gu, G. Song, S. Wang, K. Jiang, Z.-G. Cheng, T. Zhu, H. Yang, K.-j. Jin, E.-J. Guo, Syntropic spin alignment at the interface between ferromagnetic and superconducting nitrides. *Nat. Sci. Rev.* **11**, nwae107 (2024).

32. S. D. Kloß, M. L. Weidemann, J. P. Attfield, Preparation of bulk-phase nitride perovskite $LaReN_3$ and topotactic reduction to $LaNiO_2$ -Type $LaReN_2$. *Angew. Chem. Int. Ed. Engl.* **60**, 22260–22264 (2021).

33. S.-H. Baek, C.-B. Eom, Epitaxial integration of perovskite-based multifunctional oxides on silicon. *Acta Mater.* **61**, 2734–2750 (2013).

34. A. K. Yadav, C. T. Nelson, S. L. Hsu, Z. Hong, J. D. Clarkson, C. M. Schlepütz, A. R. Damodaran, P. Shafer, E. Arenholz, L. R. Dedon, D. Chen, A. Vishwanath, A. M. Minor, L. Q. Chen, J. F. Scott, L. W. Martin, R. Ramesh, Observation of polar vortices in oxide superlattices. *Nature* **530**, 198–201 (2016).

35. J. F. Scott, Applications of modern ferroelectrics. *Science* **315**, 954–959 (2007).

36. K. J. Choi, M. Biegalski, Y. L. Li, A. Sharan, J. Schubert, R. Uecker, P. Reiche, Y. B. Chen, X. Q. Pan, V. Gopalan, L.-Q. Chen, D. G. Schlom, C. B. Eom, Enhancement of ferroelectricity in strained $BaTiO_3$ thin films. *Science* **306**, 1005–1009 (2004).

37. E. J. Guo, K. Dorr, A. Herklotz, Strain controlled ferroelectric switching time of $BiFeO_3$ capacitors. *Appl. Phys. Lett.* **101**, 242908 (2012).

38. Y. Kim, A. Kumar, O. Ovchinnikov, S. Jesse, H. Han, D. Pantel, I. Vrejoiu, W. Lee, D. Hesse, M. Alex, S. V. Kalinin, First-order reversal curve probing of spatially resolved polarization switching dynamics in ferroelectric nanocapacitors. *ACS Nano* **6**, 491–500 (2012).

39. A. Stamm, D. J. Kim, H. Lu, C. W. Bark, C. B. Eom, A. Gruverman, Polarization relaxation kinetics in ultrathin ferroelectric capacitors. *Appl. Phys. Lett.* **102**, 092901 (2013).

40. Q. Yang, J. Hu, Y.-W. Fang, Y. Jia, R. Yang, S. Deng, Y. Lu, O. Dieguez, L. Fan, D. Zheng, X. Zhang, Y. Dong, Z. Luo, Z. Wang, H. Wang, M. Sui, X. Xing, J. Chen, J. Tian, L. Zhang, Ferroelectricity in layered bismuth oxide down to 1 nanometer. *Science* **379**, 1218–1224 (2023).

41. J. Gou, H. Bai, X. Zhang, Y. L. Huang, S. Duan, A. Ariando, S. A. Yang, L. Chen, Y. Lu, A. T. S. Wee, Two-dimensional ferroelectricity in a single-element bismuth monolayer. *Nature* **617**, 67–72 (2023).

42. W. Li, X. Zhang, J. Yang, S. Zhou, C. Song, P. Cheng, Y.-Q. Zhang, B. Feng, Z. Wang, Y. Lu, K. Wu, L. Chen, Emergence of ferroelectricity in a nonferroelectric monolayer. *Nat. Commun.* **14**, 2757 (2023).

43. M. Weidemann, D. Werhahn, C. Mayer, S. Kläger, C. Ritter, P. Manuel, J. P. Attfield, S. D. Kloß, High-pressure synthesis of Ruddlesden-Popper nitrides. *Nat. Chem.* **16**, 1723–1731 (2024).

44. H. Guo, Y. Huang, K. Jin, Q. Zhou, H. B. Lu, L. Liu, Y. Zhou, B. Cheng, Z. Chen, Temperature effect on carrier transport characteristics in $SrTiO_{3-\delta}/Si_{p-n}$ heterojunction. *Appl. Phys. Lett.* **86**, 123502 (2005).

45. H. F. Tian, H. X. Yang, H. R. Zhang, Y. Li, H. B. Lu, J. Q. Li, Interface of epitaxial $SrTiO_3$ on silicon characterized by transmission electron microscopy, electron energy loss spectroscopy, and electron holography. *Phys. Rev. B* **73**, 075325 (2006).

46. Z. Li, X. Guo, H. B. Lu, Z. Zhang, D. Song, S. Cheng, M. Bosman, J. Zhu, Z. Dong, W. Zhu, An epitaxial ferroelectric tunnel junction on silicon. *Adv. Mater.* **26**, 7185–7189 (2014).

47. P. Hohenberg, W. Kohn, Inhomogeneous electron gas. *Phys. Rev.* **136**, B864–B871 (1964).

48. W. Kohn, L. J. Sham, Self-consistent equations including exchange and correlation effects. *Phys. Rev.* **140**, A1133–A1138 (1965).

49. J. P. Perdew, A. Ruzsinszky, G. I. Csonka, O. A. Vydrov, G. E. Scuseria, L. A. Constantin, X. Zhou, K. Burke, Restoring the density-gradient expansion for exchange in solids and surfaces. *Phys. Rev. Lett.* **100**, 136406 (2008).

50. J. Heyd, G. E. Scuseria, M. Ernzerhof, Hybrid functionals based on a screened Coulomb potential. *J. Chem. Phys.* **118**, 8207–8215 (2003).

51. E. Kroumova, M. I. Aroyo, J. M. Perez-Mato, S. Ivantchev, J. M. Igartu, H. Wondratschek, PSEUDO: A program for a pseudosymmetry search. *J. Appl. Cryst.* **34**, 783–784 (2001).

52. C. Capillas, M. I. Aroyo, J. M. Perez-Mato, Methods for pseudosymmetry evaluation: A comparison between the atomic displacements and electron density approaches. *Z. Krist.* **220**, 691–699 (2005).

53. C. Capillas, E. S. Tasci, G. de la Flor, D. Orobengoa, J. M. Perez-Mato, M. I. Aroyo, A new computer tool at the Bilbao crystallographic server to detect and characterize pseudosymmetry. *Z. Krist.* **226**, 186–196 (2011).

54. D. Sheppard, P. Xiao, W. Chemelewski, D. D. Johnson, G. Henkelman, A generalized solid-state nudged elastic band method. *J. Chem. Phys.* **136**, 074103 (2012).

55. D. Sheppard, G. Henkelman, Paths to which the nudged elastic band converges. *J. Comp. Chem.* **32**, 1769–1771 (2011).

56. A. N. Kolmogorov, Statistical theory of metal crystallization. *Izv. Akad. Nauk SSSR Ser. Math.* **3**, 355 (1937).

57. M. Avrami, Kinetics of phase change. II transformation—time relations for random distribution of nuclei. *J. Chem. Phys.* **8**, 212–224 (1940).